ChemComm

Accepted Manuscript

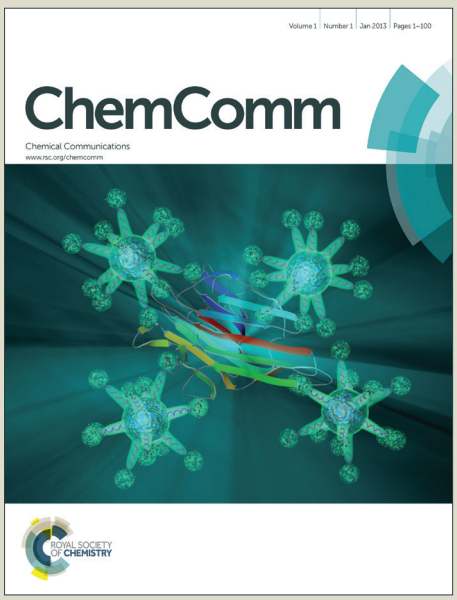

ROYAL SOCIETY OF CHEMISTRY

www.rsc.org/chemcomm

Journal Name

RSCPublishing

COMMUNICATION

Investigation of facet-dependent performance of α-Fe_2O_3 nanocrystals for heavy metals determination by stripping voltammetry

Cite this: DOI: 10.1039/x0xx00000x

Wei-Hong Xu,[‡a] Qiang-Qiang Meng,[‡b] Chao Gao,[a] Jing Wang,[a] Qun-Xiang Li,[*b] Jin-Huai Liu,[a] and Xing-Jiu Huang[*a]

Received 00th January 2012,
Accepted 00th January 2012

DOI: 10.1039/x0xx00000x

www.rsc.org/

We find that the electrochemical performances of these α-Fe_2O_3 nanostructures depend on their exposed facets for the first time. Density functional theory calculations are carried out to better and scientifically understand the effect of different exposed facets from the atomic-scale level.

It is well-known that different facets of a single-crystalline material display different geometric and electronic structures, thus endowing them with distinctive properties.[1] Recently, much attention has been focused on the facet-controlled fabrication of single-crystalline materials with well-defined morphologies due to their facet-dependent catalytic properties, such as BiOCl,[1] α-Fe_2O_3 nanostructures,[2] TiO_2,[3] gold nanostrucures,[4] and AgBr nanocrystals.[5] However, few studies have been carried out on the crystal plane effect in electrochemical detection, especially detection of heavy metal ions (HMIs). It should be noted that some of the successful coatings on modified electrodes show dramatically increased currents and increased sensitivity, simply attributing to the increased microscopic surface area or high surface free energy.[6] In fact, the facet is an important factor for modifiers, because surface atom arrangement and unsaturated dangling bonds intrinsically determine the adsorption of ion and ion transport.[3] Hence, investigation of facet-dependent performance of nanocrystals for HMIs determination by stripping voltammetry is of significance to better and scientifically understand the effect of modifiers.

In this work, we for the first time report the stripping voltammetry for sensitive and selective identification of Pb^{2+} using three types of α-Fe_2O_3 nanostructures, namely nanocubes, nanoplates, and nanorods. Density functional theory (DFT) calculations at the atomic level are expected to provide insightful information on the interaction between Pb and different exposed facets of α-Fe_2O_3 nanostructures for scientific understanding of the facet effect on stripping voltammetry.

Fig. 1a shows a representative transmission electron microscopy (TEM) image of square-shaped α-Fe_2O_3 nanocubes with an average size of about 25 nm. A high-resolution TEM (HRTEM) image (Fig. 1b) and corresponding fast Fourier transforms (FFT; inset in Fig. 1b) obviously demonstrate that the cubes are pseudocubic shape, the lattice fringes of two adjacent lateral facets are 0.36 nm, and the dihedral angle is 86°, corresponding to {012} plane.[2] Fig. 1c demonstrates a TEM image of nanoplates with a well-defined hexagonal shape. The width of the nanoplates is determined to be about 130 nm, and the ratio of the width and thickness is about 8-10 based on TEM analysis (Fig. 1c and Fig. S2). HRTEM (Fig. 1d) and corresponding FFT (inset in Fig. 1d) reveal the highly crystalline nature of the nanoplates. The lattice fringes with an interplanar lattice spacing of 0.25 nm are in agreement with (110), (-120), and (-210) planes, respectively.[2] On the basis of the symmetries

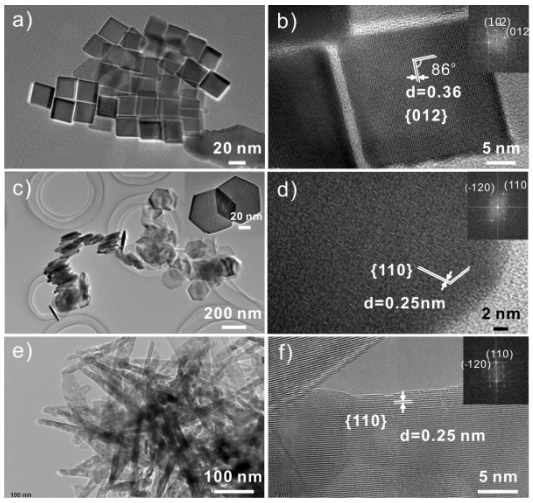

Fig. 1 Representative TEM and HRTEM images of the three types of α-Fe_2O_3 nanostructures: a, b) α-Fe_2O_3 nanocubes. c, d) α-Fe_2O_3 nanoplates. e, f) α-Fe_2O_3 nanorods. Inset in panel 1c: A TEM image at high magnification. Insets in Figure 1b, 1d, and 1f are the corresponding FFT patterns.

of α-Fe_2O_3 nanoplates, the bottom and top surfaces of the nanoplates are identified as {001} facets. TEM image (Fig. 1e) demonstrates that the α-Fe_2O_3 nanorods possess porous structure with an average diameter of about 10-20 nm and a length of about 200 nm.[7] HRTEM images (Fig. 1f) and FFT pattern (inset in Fig. 1f) indicate the lattice fringes with interplanar lattice spacing of 0.25 nm corresponding to the {110} planes. On the basis of the above analysis, α-Fe_2O_3 nanocubes, nanoplates, and nanorods provide crystallographically dominant facets of {012}, {001}, and {110}, respectively,[2] which are expected to have different electrochemical performance. The physical parameters of the α-Fe_2O_3 nanostructures, including dimensions, specific surface areas, and dominant facets are summarized in Table S1.

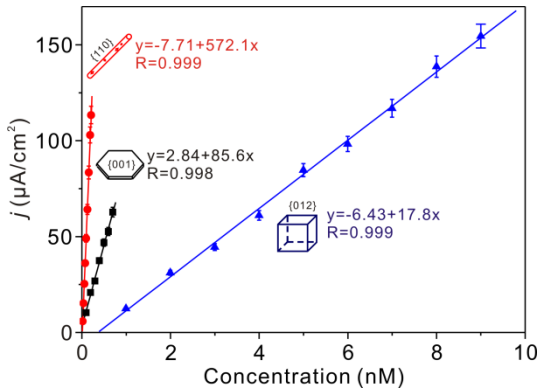

Fig. 2 Calibration plots of α-Fe_2O_3 nanocubes, nanoplates, and nanorods modified GCE for analysis of Pb^{2+} in different concentration ranges. Supporting electrolyte: 0.1 M NaAc-HAc solution (pH 5.0); deposition potential, -1.2 V (vs.SCE (saturated calomel electrode)); deposition time, 120 s; amplitude, 25 mV; increment potential, 4 mV; frequency, 15 Hz.

To distinguish the electroanalysis properties of different exposed facets of α-Fe_2O_3 nanocrystals, Pb^{2+} was chosen as a HMIs-representative probe for detailed investigation. Fig. 2 demonstrates that the current densities increase linearly versus the Pb^{2+} concentrations. For nanocubes modified glassy carbon electrode (GCE), the linearization equation is j/(μA cm^{-2}) = -6.43(±0.32) + 17.8(±0.71) c/nM. And for nanoplates modified GCE, the linearization equation is j/(μA cm^{-2}) = 2.84(±0.13) + 85.6(±3.85) c/nM. While for nanorods modified GCE, the linearization equation is j/(μA cm^{-2}) = -7.71(±0.28) + 572.1(±14.87) c/nM. The results indicate that α-Fe_2O_3 nanorods {110} facets exhibit better electrochemical detection performance than nanoplates {001} and nanocubes {012} modified GCE. The sensitivity of α-Fe_2O_3 nanorods modified GCE (572.1 μA cm^{-2}/nM) is over 6 times that of nanoplates (85.6 μA cm^{-2}/nM), and over 32 times that of nanocubes (17.8 μA cm^{-2}/nM). It is important to mention that we have calculated the active electrode surface of three types of α-Fe_2O_3 according to the Randles-Sevcik equation (see Supplementary Information, SI).[8] The electrochemical sensitivities are obtained by eliminating the effects of the active electrode surface of the three nanostructures. The limit of detection (LOD) as low as 0.41 nM, 0.045 nM and 0.0090 nM (3σ method, see SI) for α-Fe_2O_3 nanocubes, nanoplates, and nanorods modified GCE, respectively, was achieved. This meets the requirements of the World Health Organization (WHO) maximum permissible limit for lead concentration in drinking water of 10 μg L^{-1}. Fig. S3a-c display detailed square wave anodic stripping voltammetry (SWASV) response of α-Fe_2O_3 nanocubes, nanoplates, and nanorods modified GCE for analysis of Pb^{2+} in different concentration ranges. SWASV response of Pb^{2+} at bare GCE is conducted as shown in Fig. S3d. It is clear that the α-Fe_2O_3 nanostructures modified electrodes show essentially the same stripping peak so that the metal is stripped from the electrode surface in all cases (not from the surface of the α-Fe_2O_3 nanostructures). Considering the non-conductive nature of α-Fe_2O_3, the different electrochemical performance of the Fe_2O_3 nanostructures should be attributed to different Pb^{2+} adsorption and diffusion abilities on the various crystal planes, as will be carefully discussed by the following adsorption experiments and calculations. Furthermore, to investigate electrochemical performances of the three types of α-Fe_2O_3 nanostructures toward other heavy metal ions, we conducted the experiments to detect Cd^{2+}, Hg^{2+}, Cu^{2+}, and Zn^{2+} stripping signals under the optimal conditions (Fig. S6). Table S2 summarizes the sensitivity and LOD for SWASV detection of Cd^{2+}, Hg^{2+}, Cu^{2+}, and Zn^{2+} metal ions at three types of α-Fe_2O_3 nanocrystals modified GCE. As seen, the nanorods show better electrochemical properties than nanoplates and nanocubes, respectively. This further verifies the effects of different exposed facets of these α-Fe_2O_3 nanostructures, which is in agreement with the discussion above.

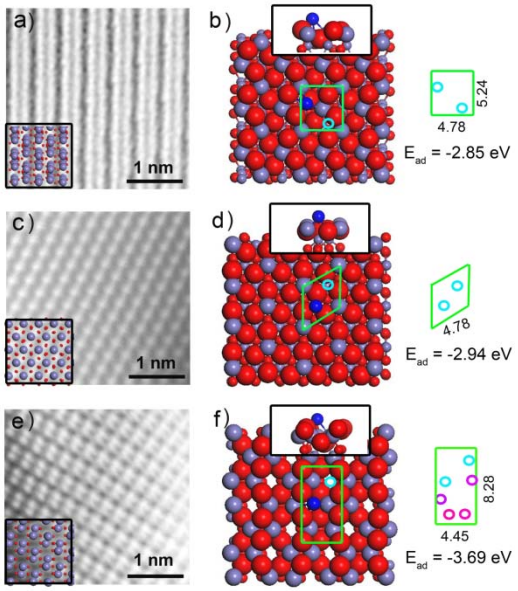

Fig. 3 Representation of HAADF atomic resolution STEM images of different crystal planes: a) (012), c) (001), e) (110), and the insert is the corresponding theoretical surface atom arrangement model. Side and top view of optimized adsorption of Pb on different α-Fe_2O_3 crystal planes: b) (012), d) (001), f) (110). Red, gray and blue spheres stand for O, Fe and Pb atoms, respectively. The right panels corresponding to b, d and f are the area of a minimum repetitive unit of adsorption sites on each surface and the cyan circles are stable adsorption sites (purple and pink are meta-stable adsorption sites with E_{ad}= -3.45 and -3.21 eV).

Additionally, we obtained the first atomic-resolution structural images of the three types of α-Fe_2O_3 nanostructures using a high-angle annular dark field scanning TEM (HAADF-STEM) with a probe-corrected electron microscope. And the experimental observations of atomic structures of different facets are in excellent agreement with theoretical model predictions, confirming the dominant exposed facets of the α-Fe_2O_3 nanostructures (Fig. 3a, c, and e, Fig. S9). Next, we have performed DFT calculations to explore the adsorption and diffusion behaviors of Pb atom on α-Fe_2O_3 (012), (001), and (110) surfaces. The adopted computational model refers to the study about Li storage capability of Ti_3C_2 and $Ti_3C_2X_2$ (X = F, OH) monolayer.[9] The adsorption configurations of Pb atom on α-Fe_2O_3 (012), (001), and (111) surfaces are optimized without any symmetry constraint shown in Fig. 3b, d, and f, respectively. For Pb/α-Fe_2O_3 (012) adsorption system, Pb atom locates at the four-fold hollow site by two O and two Fe surface atoms, and two Pb-O bond lengths are 2.35 and 2.87 Å while two Pb-Fe distances are 2.83 and 2.74 Å, respectively. The Pb atom is three-coordinated by three O atoms of α-Fe_2O_3 (001) surface, and the Pb-O bond length is 2.36 Å. For Pb/α-Fe_2O_3 (110) adsorption system, Pb atom is four-coordinated by two O (one O atom is two–coordinated while the other is three-coordinated) and two Fe atoms of α-Fe_2O_3 (110) surface, and two Pb-O bond lengths are 2.28 and 2.33 Å, and two Pb-Fe distances are 2.78 and 3.19 Å. The calculated adsorption energy of Pb atom on α-Fe_2O_3 (110) surface is -3.69 eV, which is larger than that on α-Fe_2O_3 (012) and (001) surface (-2.85 and -2.94 eV), respectively. The difference of the predicted adsorption energy for Pb on α-Fe_2O_3 different surfaces mainly originates from the relative Pb-O bond length and the number of O coordination. It means that α-Fe_2O_3 (110) plane is a more reactive and strong Pb-substrate interaction surface, (001) and (012) are the next and last, respectively. We also have examined the full-coverage of Pb on α-Fe_2O_3 (012), (001), and (110) surfaces, and the corresponding adsorption energies are predicted to be -2.39, -2.51, and -3.11eV, respectively. It is clear that they are consistent with the calculated results for low-coverage of Pb on α-Fe_2O_3 facets (-2.85, -2.94 eV and -3.69 eV for (012), (001), and (110) surfaces). On the other hand, we know that the meta-stable adsorption energies of Pb on α-Fe_2O_3 (110) surface are -3.45 and -3.21 eV, which are also larger than those of Pb/α-Fe_2O_3 (012) and (001) surfaces. As shown in the right panels corresponding to Fig. 3b, d and f, there are more adsorption sites per unit area of (110) plane. There are two equivalent stable adsorption sites within repetitive unit cell of α-Fe_2O_3 (012) and (001) plane, but the area of the repetitive unit cell of (001) plane is smaller than that of (012) plane, which means that there are more adsorption sites on (001) plane than on (012) plane. Based on the analysis of adsorption energy and the density of Pb adsorption sites, we can find that the adsorption ability order for Pb on these crystal planes follows {012} < {001} < {110}. This is consistent with the experimental results about adsorption (see Fig. S5). Furthermore, the STEM- EDS elemental mapping (see Fig. S7 and S8) reveals that Pb adsorption amount on different exposed facets are also ranked in the following order: {012} < {001} < {110}. The diffusion energy barriers of Pb on α-Fe_2O_3 (012), (001) and (110) surfaces are also calculated (Fig. S10), and Pb can effectively diffuse on these crystal planes under the experimental conditions. Thus, the selective adsorption of Pb on different exposed crystal facets is attributed to the selective electrochemical response, which is the determining factor in detection of HMIs for α-Fe_2O_3 nanostructures modified GCE.

In summary, we find that the exposed facet of α-Fe_2O_3 nanostructures including nanocubes, nanoplates, and nanorods with crystallographically dominant facets of {012}, {001}, and {110}, respectively, has a significant influence on its electrochemical performances toward Pb^{2+}, and the electrochemical sensitivity of {110}-bound α-Fe_2O_3 nanorods showed about 6-fold and 32-fold of that for nanoplates and nanocubes modified GCE, respectively. The finding is supported by DFT calculations. With our combined experimental and theoretical efforts, we are able to provide a new route to realize the improved sensitivity in electrochemical sensing of toxic metal ions.

This research was supported by the National Basic Research Program of China (2011CB933700, and 2011CB921404).

Notes and references

[a]Research Center for Biomimetic Functional Materials and Sensing Devices, Institute of Intelligent Machines, Chinese Academy of Sciences, Hefei, 230031, P. R. China. E-mail: xingjiuhuang@iim.ac.cn
[b]Hefei National Laboratory for Physical Sciences at the Microscale, University of Science and Technology of China, Hefei, 230026, P. R. China. E-mail: liqun@ustc.edu.cn

†Electronic Supplementary Information (ESI) available: XRD patterns, TEM image of α-Fe_2O_3 nanoplates, N_2 adsorption-desorption isotherms, Adsorption capacity for Pb on α-Fe_2O_3 nanostructures, STEM-EDS elemental mapping images of α-Fe_2O_3 nanostructures, EDX spectra, and computational details. See DOI: 10.1039/b000000x/

‡ These authors contributed equally.

1 J. Jiang, K. Zhao, X. Y. Xiao and L. Z. Zhang, *J. Am. Chem. Soc.*, 2012, **134**, 4473-4476.
2 X. M. Zhou, J. Y. Lan, G. Liu, K. Deng, Y. L. Yang, G. J. Nie, J. G. Yu and L. J. Zhi, *Angew. Chem. Int. Ed.*, 2012, **51**, 178-182.
3 F. Zuo, K. Bozhilov, R. J. Dillon, L. Wang, P. Smith, X. Zhao, C. Bardeen and P. Y. Feng, *Angew. Chem. Int. Ed.*, 2012, **51**, 6223-6226.
4 C. Y. Chiu, P. J. Chung, K. U. Lao, C. W. Liao and M. H. Huang, *J. Phys. Chem. C*, 2012, **116**, 23757-23763.
5 H. Wang, J. T. Yang, X. L. Li, H. Z. Zhang, J. H. Li and L. Guo, *Small*, 2012, **8**, 2802-2806.
6 L. Wang, W. H. Xu, R. Yang, T. Zhou, D. Hou, X. Zheng, J. H. Liu and X. J. Huang, *Anal. Chem.*, 2013, **85**, 3984-3990.
7 Y. Wang, J. L. Cao, S. R. Wang, X. Z. Guo, J. Zhang, H. J. Xia, S. M. Zhang and S. H. Wu, *J. Phys. Chem. C*, 2008, **112**, 17804-17808.
8 D. Du, M. H. Wang, J. M. Zhang, H. Cai, H. Y. Tu and A. D. Zhang, *Electrochem. Commun.*, 2008, **10**, 85-89.
9 Q. Tang, Z. Zhou and P. W. Shen, *J. Am. Chem. Soc.*, 2012, **134**, 16909-16916.